Multiple-Doppler Radar Observations of the Evolution of Vorticity Extrema in a Convective Boundary Layer

PAUL MARKOWSKI AND CHRISTINA HANNON

Department of Meteorology, The Pennsylvania State University, University Park, Pennsylvania

ABSTRACT

Overdetermined, dual-Doppler wind syntheses are used to document the evolution, structure, and dynamics of vertical vorticity extrema observed in a convective boundary layer during the 12 June 2002 International H_2O Project (IHOP) mission. Discrete vertical vorticity extrema having horizontal scales of 1–2 km can be observed continuously for periods exceeding an hour. The evolution of the vorticity field is characterized by complex interactions among vorticity extrema and between the vertical vorticity and vertical velocity fields. The most prominent vorticity maxima have amplitudes of approximately 0.01 s^{-1} and are associated with retrieved pressure deficits of order 0.1 mb. The vorticity extrema weaken with height and tilt in the presence of vertical wind shear. Advection and propagation both contribute substantially to the motion of the vorticity extrema.

Amplifications of vertical vorticity are closely linked to the intensification of updrafts. Both stretching and tilting can contribute significantly to the vorticity budgets of the air parcels comprising the vorticity extrema, and their relative importance varies with elevation, evolutionary stage, and from one vorticity extremum to another. It is therefore difficult to generalize about the dynamics of the vorticity extrema. It also is difficult to generalize about the helicity of the vorticity maxima and suppression of mixing for similar reasons. The weakening of vertical vorticity extrema is closely tied to the weakening of updrafts. In some cases, downward-directed vertical pressure gradient forces due to vertical gradients of rotation bring about updraft weakening and vorticity demise. An improved understanding of the nature of boundary layer vortices could have large relevance to convection initiation owing to feedbacks between vertical velocity and vorticity.

1. Introduction and motivation

The ubiquity of vortices in convective boundary layers is apparent in many observations and simulations (e.g., Carroll and Ryan 1970; Maxworthy 1973; Cortese and Balachandar 1993; MacPherson and Betts 1997; Schneider and Lilly 1999; Kanak et al. 2000). For example, dust devils are common on sunny days, at least when land surface characteristics allow such vortices to be manifest visually (e.g., Kaimal and Businger 1970; Hess and Spillane 1990; Snow and McClelland 1990). Radar observations of the boundary layer also commonly reveal vortices, probably having a spatial scale larger than dust devils (e.g., Wilson et al. 1992). Some boundary layer vortices have been observed to be as-sociated with cloud development (e.g., Atkins et al. 1995, 1998). These latter observations have led some to hypothesize that boundary layer vortices are an important aspect of convection initiation (e.g., Kingsmill 1995; Lee and Finley 2000).

Theoretical studies have investigated the formation of vertical vortices within corridors of horizontal wind shear that arise from the instability of shear flows and vortex sheets (e.g., Miles and Howard 1964; Kundu 1990, 391–395). Such processes have been hypothesized to be responsible for the development of boundary layer vertical vortices in some observational studies (e.g., Mueller and Carbone 1987; Kingsmill 1995; Roberts and Wilson 1995). In other cases, vorticity stretching (e.g., Wilson et al. 1992) and tilting of horizontal vorticity (e.g., Atkins et al. 1995) have been observed to be the dominant contributors to vertical vorticity amplification. Large-eddy simulations of convective boundary layers also have examined the formation of vortices. For example, Kanak et al. (2000) found that

Corresponding author address: Dr. Paul Markowski, The Pennsylvania State University, 503 Walker Building, University Park, PA 16802.
E-mail: pmarkowski@psu.edu

local vertical vortices tended to arise within vertical velocity maxima. In their simulations, as well as in idealized, inviscid simulations of isolated buoyant elements by Shapiro and Kanak (2002), no mean wind was prescribed. Kanak et al. (2000) conjectured and Shapiro and Kanak (2002) deduced that horizontal vorticity initially was generated by the density gradients associated with the thermals, and this horizontal vorticity subsequently was tilted by horizontal gradients of vertical velocity to yield vertical vorticity.

The dynamics, origin, and evolution of boundary layer vortices could have large relevance to convection initiation owing to the feedbacks between vertical velocity and vorticity. These feedbacks have been studied fairly extensively in theoretical and numerical modeling studies of deep, moist convection (Klemp 1987), but the possibility of similar interactions in boundary layer updrafts, and their ramifications for convection initiation, remain largely unexplored. Prior observational studies of boundary layer vortices often have been limited by their spatial and temporal resolution, which is considerably coarser than what has been available in large-eddy simulations.[1] It is this fact that motivates the present paper.

The purpose of this paper is to use high-resolution [90 s in time, $O(1$ km) in space], three-dimensional wind syntheses derived from Doppler radar data to document the finescale structure and evolution of boundary layer vertical vorticity extrema, in addition to the dynamical processes playing a role in the amplification and demise of the vorticity extrema. The radar data were obtained on 12 June 2002 in northwestern Oklahoma during the International H_2O Project (IHOP; Weckwerth et al. 2004). A more descriptive overview of the dataset and analysis techniques is provided in section 2. The major observations are presented in sections 3–5. Section 6 contains conclusions and some final remarks.

2. Overview and methods

During the afternoon of 12 June 2002, four mobile radars were dispatched to northwestern Oklahoma in anticipation of convection initiation in the proximity of the intersection of an outflow boundary and a dryline (Fig. 1). Shallow cumulus clouds were observed within the data analysis region for the first 90 min of the deployment. Some towering cumulus clouds developed

---

[1] Vortices are difficult to define mathematically. Popular definitions often require closed streamlines or local vorticity anomalies, but even these definitions have significant limitations (Lugt 1979). We attempt to avoid these issues entirely by restricting our terminology to vorticity extrema, maxima, and minima hereafter.

2103 UTC 12 June 2002
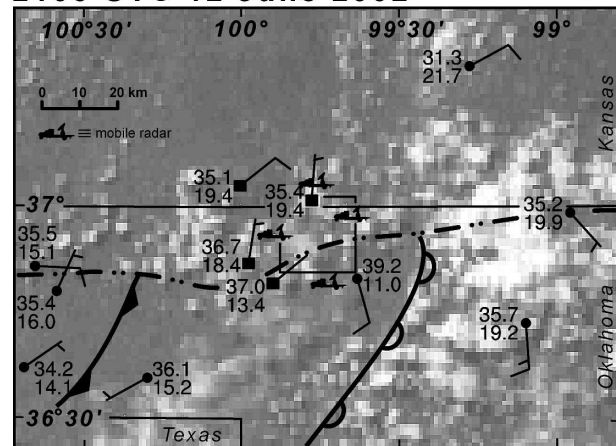
FIG. 1. Surface observations and visible satellite imagery at 2103 UTC 12 Jun 2002 in the region surrounding the radar analysis domain. The box near the center of the image outlines the mobile radar analysis region, and the four radar truck icons within this region indicate the positions of the mobile radars. Temperature (°C), dewpoint temperature (°C), wind speed (half barb—2.5 m s^{-1}; full barb—5 m s^{-1}), and wind direction are plotted in the station models. Station models having a filled square at the base of the wind barb are observations obtained from mobile mesonets. The bold dash–dot line indicates an outflow boundary, the bold line with filled barbs indicate a cold front, and the bold line with unfilled scallops indicates a dryline.

along the outflow boundary during the 2100–2130 UTC time period, and at the same time, along the dryline to the east, cumulonimbus clouds were initiated. A more complete synoptic and mesoscale summary of this case is provided by Markowski et al. (2006).

Radar data were collected continuously from 1936 to 2130 UTC. Three of the mobile radars [two Doppler On Wheels (DOWs) radars and an X-band dual-polarimetric radar (XPOL)] were similar to those described by Wurman et al. (1997). The wavelength, stationary half-power beamwidth, and Nyquist velocity were 3 cm, 0.93°, and 16.0 m s^{-1}, respectively. Volumes were completed every 90 s, during which time 16 elevation angles were scanned from 0.5° to 14.5°. The azimuth interval between each ray was 0.7°. Within the analysis region, the data spacing (note the oversampling implied by the sampling intervals in azimuth and elevation angle) was approximately 70–250 m in the horizontal and 50–300 m in the vertical. The fourth mobile radar [Shared Mobile Atmospheric Research and Teaching (SMART) Radar] has been described by Biggerstaff and Guynes (2000). The wavelength, stationary half-power beamwidth, and Nyquist velocity were 5 cm, 1.5°, and 14.6 m s^{-1}, respectively. Volumes were completed every 180 s, during which time 15 elevation angles were scanned from 0.5° to 25.2°. The
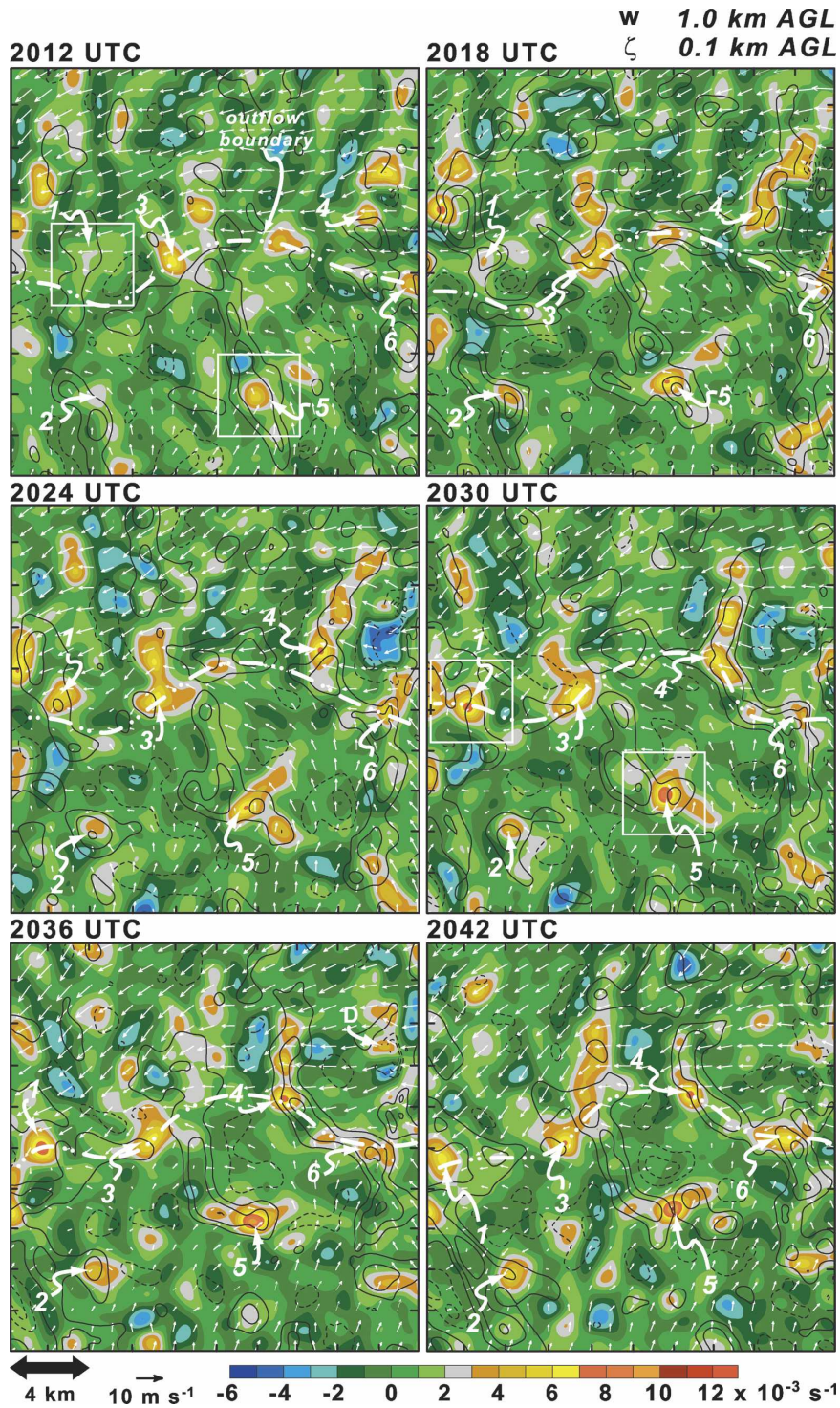
FIG. 2. Horizontal cross sections of vertical velocity, ζ, at 0.1 km above ground level (shaded, see scale at bottom) and vertical velocity, w, at 1.0 km (contoured at 1 m s^{-1} intervals, negative contours are dashed, and the 0 m s^{-1} contour has been suppressed) at 6-min intervals from 2012 to 2042 UTC. Horizontal wind vectors also appear on each panel (the tail of each vector is located at every 10th grid point). The position of the outflow boundary is subjectively analyzed with the dash–dot line. The vorticity maxima discussed in the text are labeled in each panel. The boundaries of the zoomed images displayed in Figs. 11–14 are indicated in the 2012 and 2030 UTC panels. The "D" in the northeastern part of the 2036 UTC panel indicates the approximate location of a long-lived, intense dust devil observed visually.
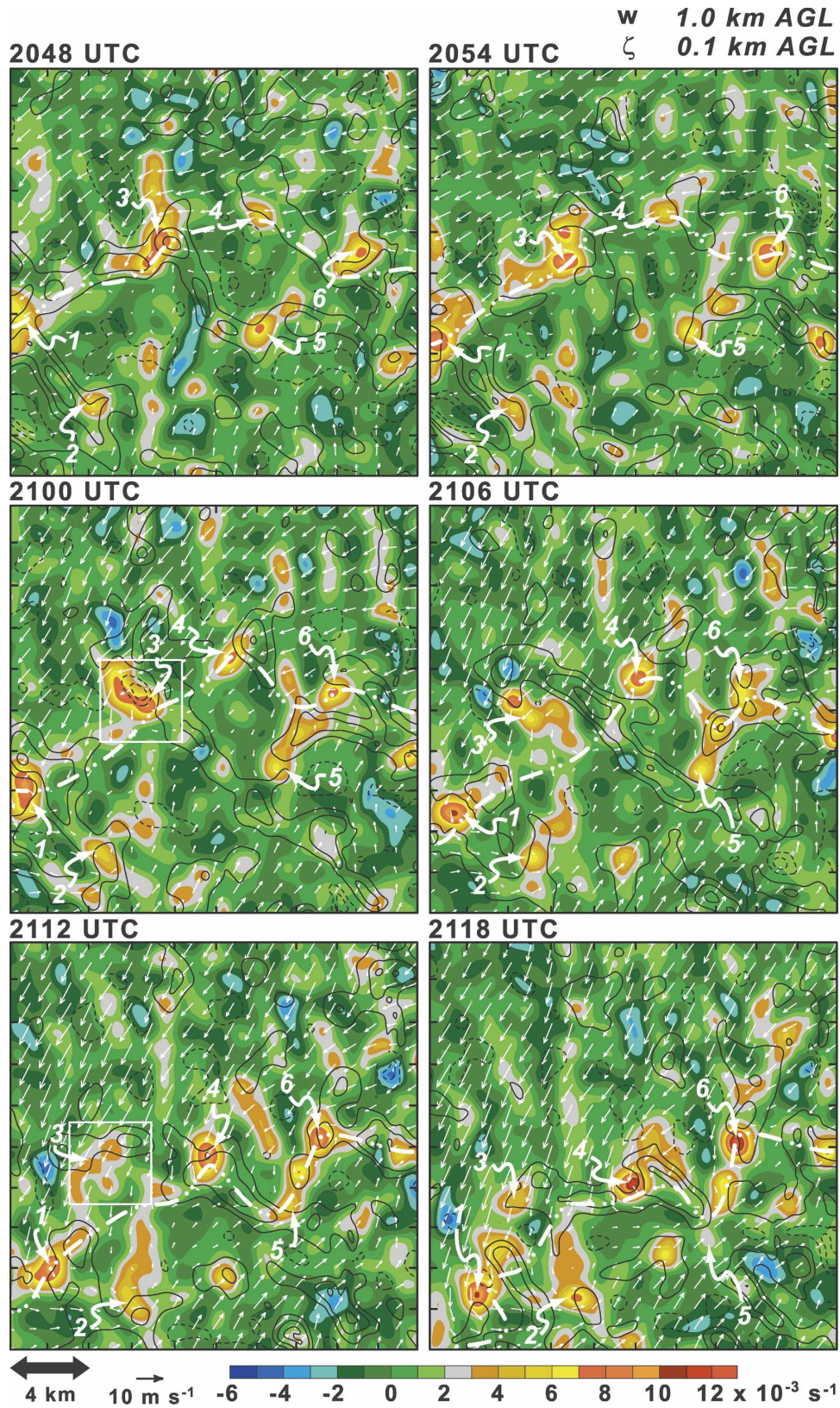
FIG. 3. As in Fig. 2, but for the period 2048–2118 UTC. The boundaries of the zoomed images displayed in Figs. 17 and 18 are indicated in the 2100 and 2112 UTC panels.

azimuth interval between each ray was 1.0°. Within the analysis region, the data spacing was approximately 70–350 m in the horizontal and 50–400 m in the vertical.

Radial velocity errors caused by low signal-to-noise ratio, second-trip echoes, sidelobes, ground clutter, and velocity aliasing were removed prior to interpolating the data to a Cartesian grid. The azimuth orientations of the radars were corrected by comparing ground clutter patterns to the known positions of landmarks visible in the clutter patterns. The orientations of two of the radars (DOW2 and XPOL) were confirmed by solar alignment scans (Arnott et al. 2003).

The grid used for the analyses presented herein is 20 × 20 × 2 km^3 (Fig. 1) and has a horizontal and vertical grid spacing of 100 m. Interpolation of the radial velocity data to the grid was accomplished with a Barnes objective analysis (Barnes 1964; Koch et al. 1983) using an isotropic, spherical weight function and smoothing parameter, κ, of 0.36 km^2. This choice of smoothing parameter yields a 25% theoretical response for features having a wavelength of 1.6 km, which is approximately 4 times the coarsest data spacing at a range of 25 km from the radars (approximately the coarsest data spacing in the dual-Doppler analysis region). This relatively conservative choice for κ follows the recommendations of Trapp and Doswell (2000). For computational reasons, data beyond a "cutoff" radius of 1.25 km from each grid point were not considered in the calculation of the weights, even though the theoretical contribution to the weight function remains nonzero and positive, albeit very small, for distances between a datum and grid point approaching infinity.

Matejka's (2002) technique was used for determining the optimal reference frame motion, which was used to remove the effects of advection from the objectively analyzed radial velocity grids. The wind syntheses were insensitive to the choice of reference frame motion, at least within a reasonable range of motions, due to the relatively fast scanning and small wind speeds. The details of this sensitivity analysis appear in Markowski et al. (2006).

The three-dimensional wind field was synthesized using the overdetermined dual-Doppler approach (e.g., Kessinger et al. 1987) and the anelastic mass continuity equation (integrated upward), rather than a direct triple- or quadruple-Doppler solution. The time resolution of the analyses is 90 s, which equals the time required for the two DOWs and XPOL to complete volumes. Thus, the three-dimensional wind syntheses alternate between a three-radar and four-radar solution, since the fourth (SMART) radar completed volumes only every 180 s. Dynamic retrievals of the pressure perturbation field also were performed, following
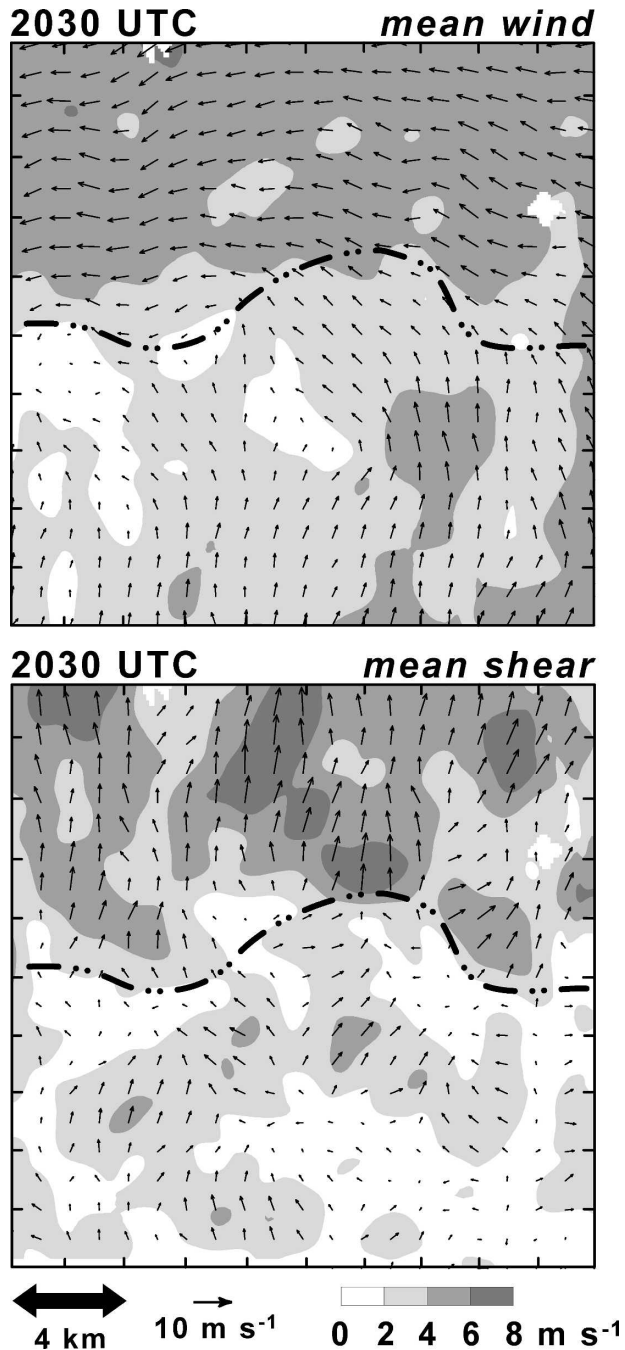
FIG. 4. (top) The 0.0–1.5-km mean wind vectors at 2030 UTC. The mean wind speed is indicated with shading. The position of the outflow boundary is indicated with the dash–dot line. (bottom) The 0.0–1.5-km mean wind shear vectors at 2030 UTC. The magnitude of the mean wind shear is indicated with shading. The position of the outflow boundary is indicated with the dash–dot line.

the technique outlined by Gal-Chen (1978). Vertical perturbation pressure gradients were obtained using the methodology proposed by Roux (1985). Additional details regarding the objective analysis approach, wind

Vorticity Maximum #5
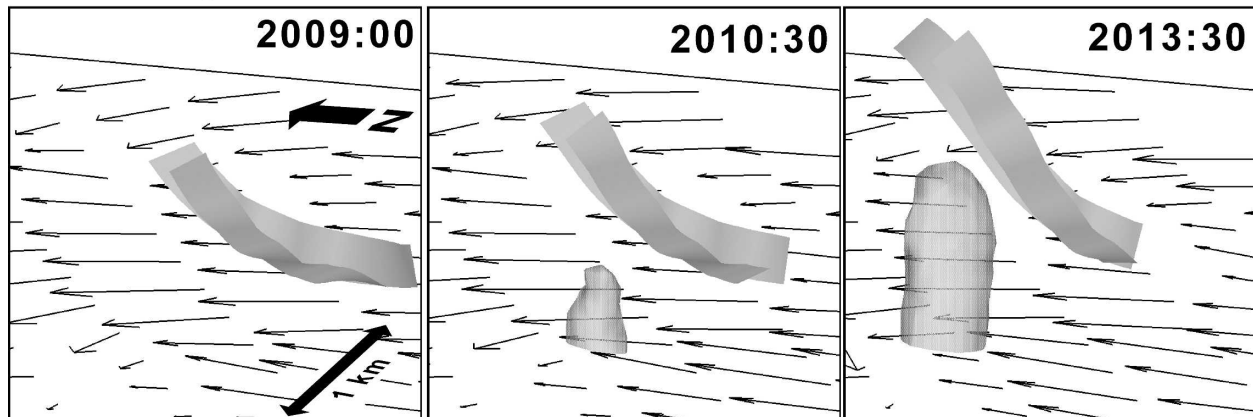
FIG. 5. The evolution of the 5×10^{-3} s^{-1} vertical vorticity isosurface (gray) associated with the intensification of vorticity maximum number 5 between 2009:00 and 2013:30 UTC. The view is from the west-southwest. Black arrows represent the horizontal wind vectors at 100 m and a few ribbons have been drawn in order to illustrate the air motions during this period.

synthesis techniques, pressure retrieval, and error analysis are presented by Markowski et al. (2006).

3. Evolution of the vertical vorticity field

Although the wind syntheses span the 1936–2130 UTC period, the proceeding analysis and discussion focuses on the 2012–2118 UTC time period. Figures 2 and 3 depict the vertical vorticity and vertical velocity fields at 6-min intervals (i.e., every fourth wind synthesis is displayed) from 2012 to 2118 UTC. Vertical vorticity maxima are observed both along the outflow boundary (e.g., the vorticity maxima identified with numbers "3" and "6" in Figs. 2 and 3) and away from the outflow boundary, both on its warm as well as its cool side (e.g., the vorticity maxima identified with numbers "2" and "5" in Figs. 2 and 3). Other vorticity maxima evolve from positions away from the outflow boundary to positions along the outflow boundary (e.g., those identified with numbers "1" and "4" in Fig. 2 between 2012 and 2030 UTC).

A few long-lived (>1 min) dust devils were witnessed by the radar operators, but it is not known what dynamical relationship, if any, these had to the vorticity maxima observed in the radar-derived wind syntheses. The location of one such dust devil is indicated in Fig. 2 at 2036 UTC. It is perhaps worth noting that the dust devil was located within a relative maximum in the radar-resolved vertical vorticity field.

The motions of the vorticity extrema are generally similar to the ambient, vertically averaged wind velocity in the vicinity of the vorticity extrema (Fig. 4a). Many extrema also are observed to propagate laterally

with respect to the ambient wind direction for brief periods of time, although there is no systematic preference for cyclonic (anticyclonic) vorticity extrema to propagate to the right (left) of the mean shear vector (Fig. 4b) as Maxworthy (1973) observed in the case of dust devils.

What is perhaps most remarkable about Figs. 2 and 3 is the time continuity of the vorticity field.[2] Vorticity extrema (e.g., those numbered 1–6 in Figs. 2 and 3) can be tracked continuously for the entire radar deployment. The vorticity extrema weaken and strengthen in time and occasionally merge with one another, but the extrema generally fail to dissipate entirely or become unidentifiable in the wind syntheses. *In other words, the very definition of the genesis and dissipation of a vorticity extremum is ambiguous*. It will be shown in section 5 that the vertical vorticity of individual air parcels entering a vorticity extremum can be traced backward in time to values approaching zero, but this does not contradict the finding that a "genesis time" and "end time" could not be defined for the vorticity extrema.

Close inspection of the vertical vorticity fields also reveals many complex interactions among vertical vorticity maxima and between the vertical vorticity and vertical velocity fields. For example, the weaker vorticity extrema occasionally are observed orbiting stronger vorticity extrema, the so-called Fujiwhara effect (Fujiwhara 1931). An example of this evolution is observed in proximity to vorticity maximum number 5 during the

---

[2] This behavior is even more apparent in electronic animations available from the corresponding author.

2012–2042 UTC period (Fig. 2). In this same region, notice how the vertical velocity field also is rearranged by the interactions between vorticity extrema. Bluestein et al. (2004) have observed similar interactions between dust devils.

During periods in which vertical vorticity amplifies, amplification first occurs near the ground and then builds upward in time (Fig. 5). Rapid amplification is preceded by updrafts; that is, vorticity amplification is a by-product of updrafts, as evidenced by the sequence of trajectories and vorticity isosurfaces in Fig. 5 (this is just one of several examples). The amplification of low-level vertical vorticity often leads to a weakening of updrafts—and occasionally induces downdrafts—in a manner reminiscent of the process attributed to occlusion downdraft formation in supercell thunderstorms (Klemp and Rotunno 1983). Examples of this evolution include vorticity maximum number 3 at 2100 UTC (Fig. 3) and vorticity maximum number 4 at 2118 UTC (Fig. 3).

The dynamical processes associated with the amplification phases of vorticity extrema, in addition to the processes associated with their demise, are investigated in much greater depth in section 5. It is perhaps humbling to see such nonlinear interactions between vorticity extrema and feedbacks to the vertical velocity field when attempting to make progress toward better understanding convection initiation, which was one motivation for IHOP and the collection of these data.

4. Characteristics of the vertical vorticity extrema

The most prominent vertical vorticity maxima, which tend to be located along the outflow boundary and within the warm sector south of the boundary, attain values of 10^{-2} s^{-1} (Figs. 2 and 3). The most prominent minima attain values of -6×10^{-3} s^{-1}. These amplitudes are less than those in the large-eddy simulations conducted by Kanak et al. (2000), but vorticity values are highly resolution dependent. The grid spacing in the radar analysis domain is approximately 3 times the horizontal grid spacing in the Kanak et al. simulations. The angular momenta associated with the strongest vorticity maxima, estimated by averaging the vertical vorticity within the area coinciding with a vorticity extremum (typically a circle with a radius of 0.5–1.0 km), range from 800 to 1300 m^2 s^{-1}, which is slightly larger than estimated by Kanak et al. in their simulations.

The magnitudes of the vorticity extrema generally decrease with height from their largest values near the surface (Fig. 6), although all of the significant vorticity extrema span the depth of the boundary layer, which is

2100 UTC
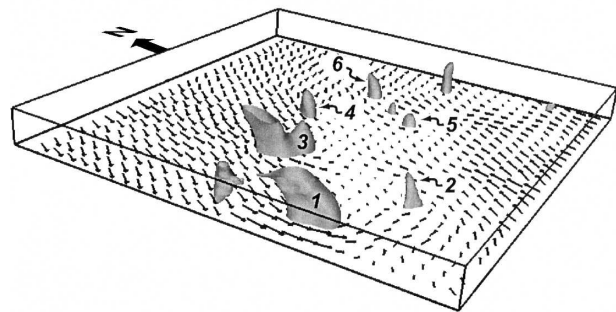
FIG. 6. The 5×10^{-3} s^{-1} vertical vorticity isosurfaces (gray) viewed from the southwest at 2100 UTC. Black arrows represent the horizontal wind vectors at 100 m. The vorticity maxima labeled 1–6 in Figs. 2 and 3 also are indicated.

approximately 2 km deep. The vertical vorticity extrema north of the outflow boundary also have some tendency to be tilted away from the vertical toward the cool side of the outflow boundary (Fig. 6), owing to the enhanced southerly vertical wind shear north of the boundary (Fig. 4b). The vertical vorticity extrema in the

2112 UTC
0.1 km AGL p' ζ
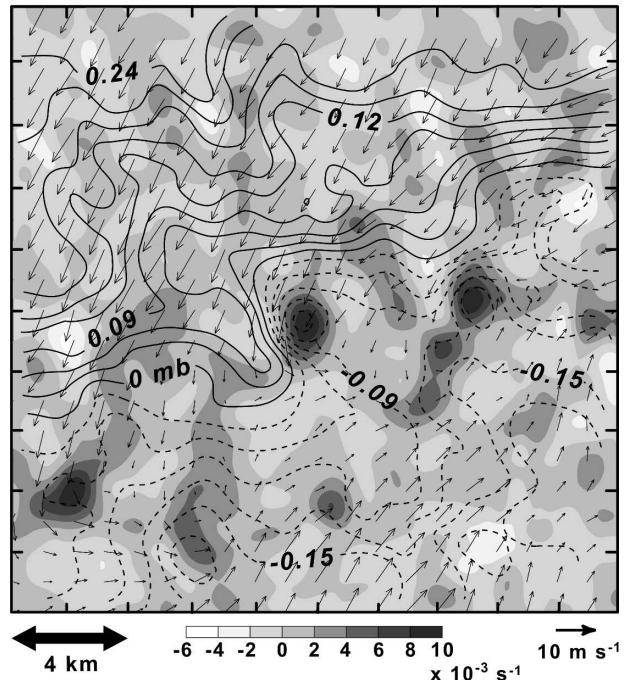
FIG. 7. Horizontal cross section of vertical vorticity, ζ, at 0.1 km (shaded, see scale at bottom) and perturbation pressure, p', at 0.1 km (contoured at 0.03-mb intervals, negative contours are dashed). Pressure perturbations are with respect to the mean pressure at 0.1 km within the analysis domain.
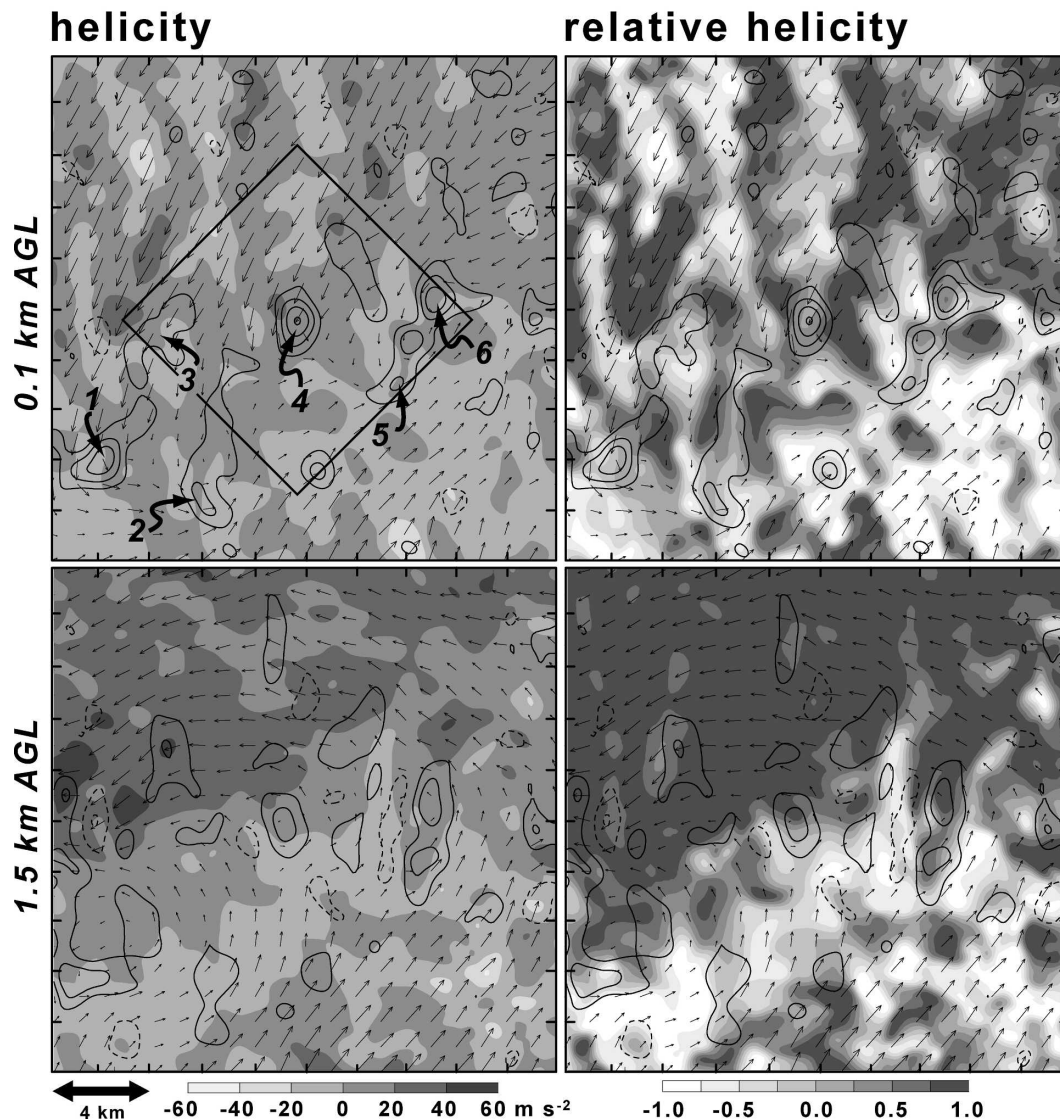
FIG. 8. Horizontal cross sections of (left) helicity ($\mathbf{v} \cdot \boldsymbol{\omega}$) (gray shades) and (right) relative helicity ($\mathbf{v} \cdot \boldsymbol{\omega}/|\mathbf{v}||\boldsymbol{\omega}|$) (gray shades) at 0.1 and 1.5 km at 2112 UTC. Vertical vorticity contours are overlaid (2.5×10^{-3} s^{-1} intervals; negative contours are dashed and the zero contour is suppressed). (top left) The diamond-shaped region indicates the locations of the cross sections shown in Fig. 9. The vorticity maxima labeled 1–6 in Fig. 3 also are indicated.

warm sector south of the outflow boundary tend to be more upright as a consequence of the weaker vertical wind shear present there.

Retrieved pressure minima are collocated with significant vorticity extrema (Fig. 7), presumably a dynamical consequence of the rotation. The amplitudes of these minima are small, with pressure deficits rarely exceeding 0.15 mb compared to the pressure in close proximity to the vorticity extrema. It should be noted that the retrieved pressure field tends to be smoother

than the vertical vorticity field;[3] therefore, it would not be surprising if the actual pressure fluctuations are considerably larger than those retrieved.

No systematic relationship between the vertical velocity and vertical vorticity fields is evident (the do-

_____

[3] The forcing for the pressure field was smoothed prior to solving the elliptic pressure equation in order to obtain a better fit of the pressure field to the wind observations (Gal-Chen and Kropfli 1984).
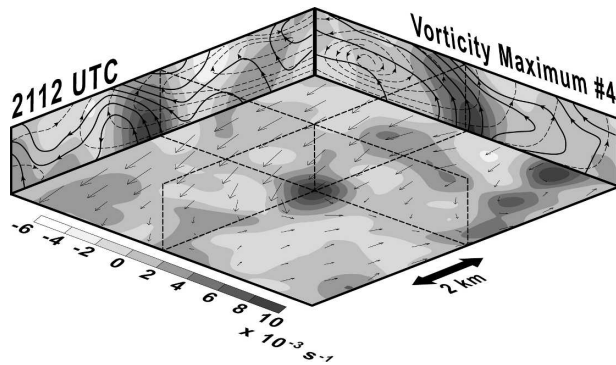
FIG. 9. Vertical cross sections through the center of vorticity maximum number 4. The horizontal cross section is at 0.1 km and encompasses the region outlined with the diamond in Fig. 8. North is at the top of the figure. The vertical vorticity field is shaded as in Fig. 7 (see legend). The horizontal wind vectors at 0.1 km also are plotted on the horizontal cross section. Vortex lines (solid) and streamlines (dashed) in the plane of the vertical cross sections are overlaid on the vertical cross sections.

main-wide linear correlation is <0.2 at all analysis times), nor can a meaningful wavelength between vorticity maxima be defined (e.g., Kingsmill 1995; Richardson et al. 2003), owing to the highly irregular spatial distribution of vorticity (e.g., Fig. 2). Some vorticity maxima are situated beneath updraft centers, others are located on the flanks of updrafts, and others are located in downdrafts (Figs. 2 and 3). It also is curious that circularly symmetric (in a horizontal plane) vorticity maxima occasionally develop beneath quasi-linear updrafts (e.g., vorticity maximum number 5 at 2012 UTC; Fig. 2).

Davies-Jones (1984) showed that the correlation between vertical velocity and vertical vorticity in an updraft or downdraft depends on whether the horizontal vorticity tilted by the draft is crosswise or streamwise in a reference frame moving with the draft. It is difficult to apply this result to the drafts herein for at least a couple of reasons. First, the simple relationship between crosswise/streamwise vorticity and the vertical velocity/vorticity correlation applies to drafts that have a circular cross section. The correlation is considerably more difficult to obtain when drafts deviate from circular symmetry as observed herein. A second complication is that the motion of the drafts is highly variable and difficult to define, even when tracking just a single draft. The drafts constantly change shape (as viewed in horizontal cross sections). Thus, determining the appropriate updraft-relative reference frame would be an arduous task.

It has been hypothesized that the importance of vorticity maxima in convection initiation could be related to their helicity and corresponding suppression of mix-

ing (e.g., Kanak et al. 2000; Pietrycha and Rasmussen 2004). If the entrainment of environmental air into an ascending plume, which tends to reduce buoyancy and potential buoyancy within the plume, can be reduced owing to the stabilizing influence of rotation (Andrè and LeSieur 1977; Lilly 1986), then vorticity maxima might be favored sites for convection initiation. There-
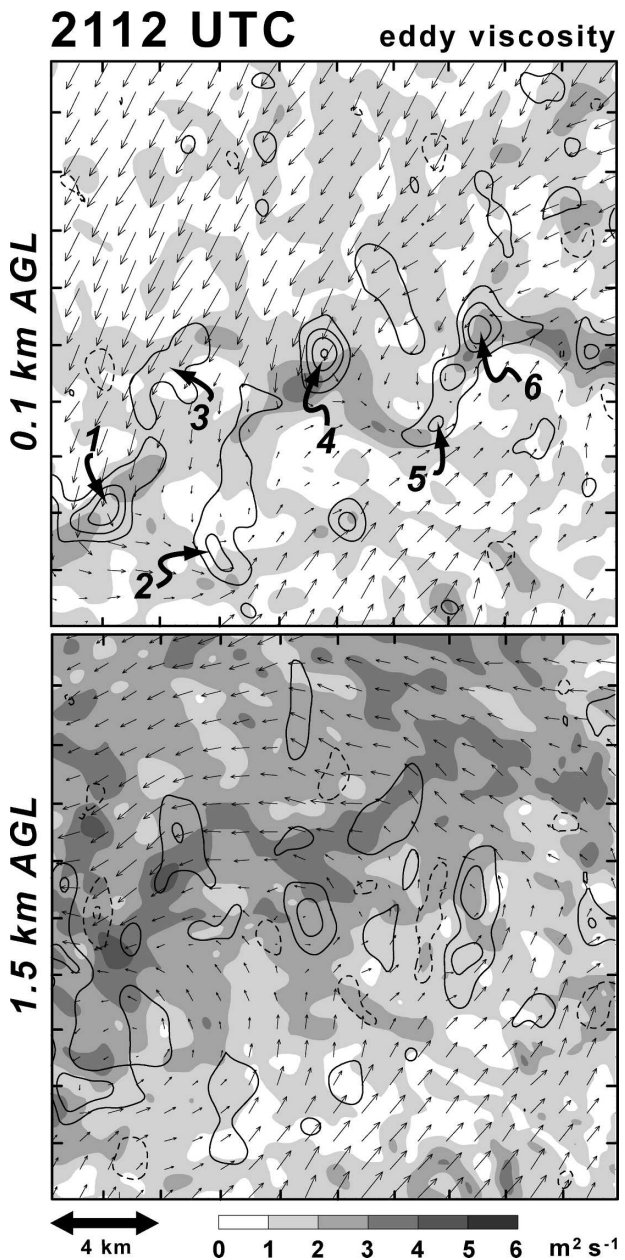
FIG. 10. Horizontal cross sections of eddy viscosity at 0.1 and 1.5 km at 2112 UTC (gray shades), with vertical vorticity contours overlaid (2.5×10^{-3} s^{-1} intervals; negative contours are dashed and the zero contour is suppressed). The vorticity maxima labeled 1–6 in Fig. 3 also are indicated.

2012 UTC   *Vorticity Maximum #1*
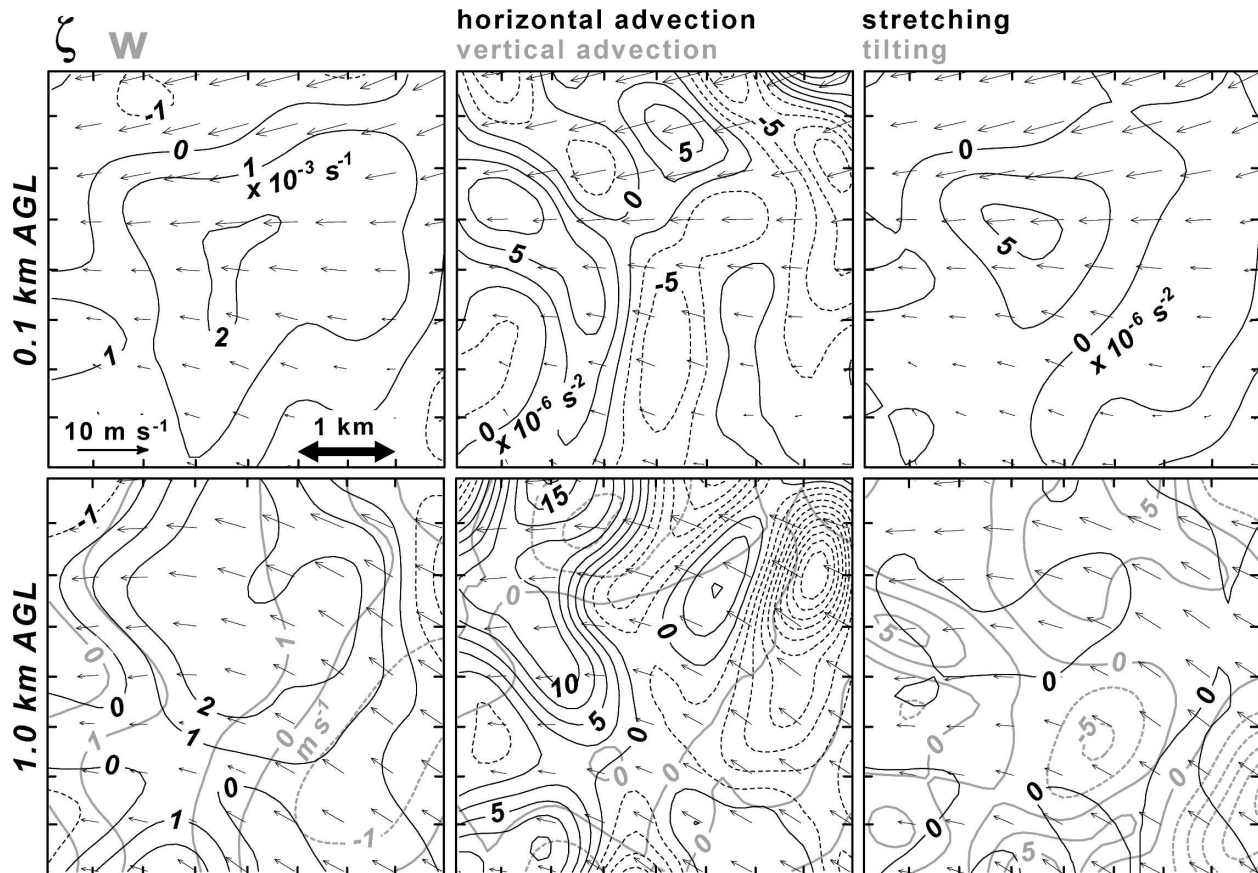
FIG. 11. (left) Horizontal cross sections of vertical vorticity, ζ, and vertical velocity, w, at (top) 0.1 and (bottom) 1.0 km in the proximity of vorticity maximum number 1 at 2012 UTC (refer to Fig. 2). Vertical vorticity (black) is contoured at 1×10^{-3} s^{-1} intervals, with negative contours dashed. Vertical velocity (gray) is contoured at 1 m s^{-1} intervals, with negative contours dashed. (center) Horizontal cross sections of horizontal and vertical advection of vertical vorticity at (top) 0.1 and (bottom) 1.0 km. Horizontal advection (black) is contoured at 2.5×10^{-6} s^{-2} intervals, with negative contours dashed. Vertical advection (gray) also is contoured at 2.5×10^{-6} s^{-2} intervals, with negative contours dashed. (right) Horizontal cross sections of vorticity stretching and tilting at (top) 0.1 and (bottom) 1.0 km. Stretching (black) is contoured at 2.5×10^{-6} s^{-2} intervals, with negative contours dashed. Tilting (gray) also is contoured at 2.5×10^{-6} s^{-2} intervals, with negative contours dashed.

fore, it is perhaps worthwhile to investigate the helicity of the synthesized wind fields.

Figure 8 displays the helicity, H,

$$H = \mathbf{v} \cdot \boldsymbol{\omega}, \tag{1}$$

and relative helicity (Lilly 1986), h,

$$h = \frac{\mathbf{v} \cdot \boldsymbol{\omega}}{|\mathbf{v}||\boldsymbol{\omega}|}, \tag{2}$$

where $\mathbf{v} = (u, v, w)$ is the three-dimensional velocity vector and $\boldsymbol{\omega} = \nabla \times \mathbf{v} = (\xi, \eta, \zeta)$ is the three-dimensional vorticity vector. The relative helicity h can have values from -1 to 1. When $h = 1$ ($h = -1$), the

vorticity is streamwise (antistreamwise), and when $h = 0$, the vorticity is crosswise. It is apparent from Figs. 8 and 9 that it is difficult to generalize about the helicity and relative helicity of vorticity maxima. The degree to which vortex lines coincide with streamlines varies from one vorticity extremum to another, and it also depends on evolutionary stage and elevation above ground. For example, vorticity maxima numbers 5 and 6 in Fig. 8 are associated with local maxima in relative helicity, whereas vorticity maximum number 4 in Fig. 8 is associated with a local minimum in relative helicity at 0.1 km and resides within a large relative helicity gradient at 1.5 km. Some vorticity maxima are associated with nearly zero or negative relative helicity (e.g., vorticity

2030 UTC   *Vorticity Maximum #1*
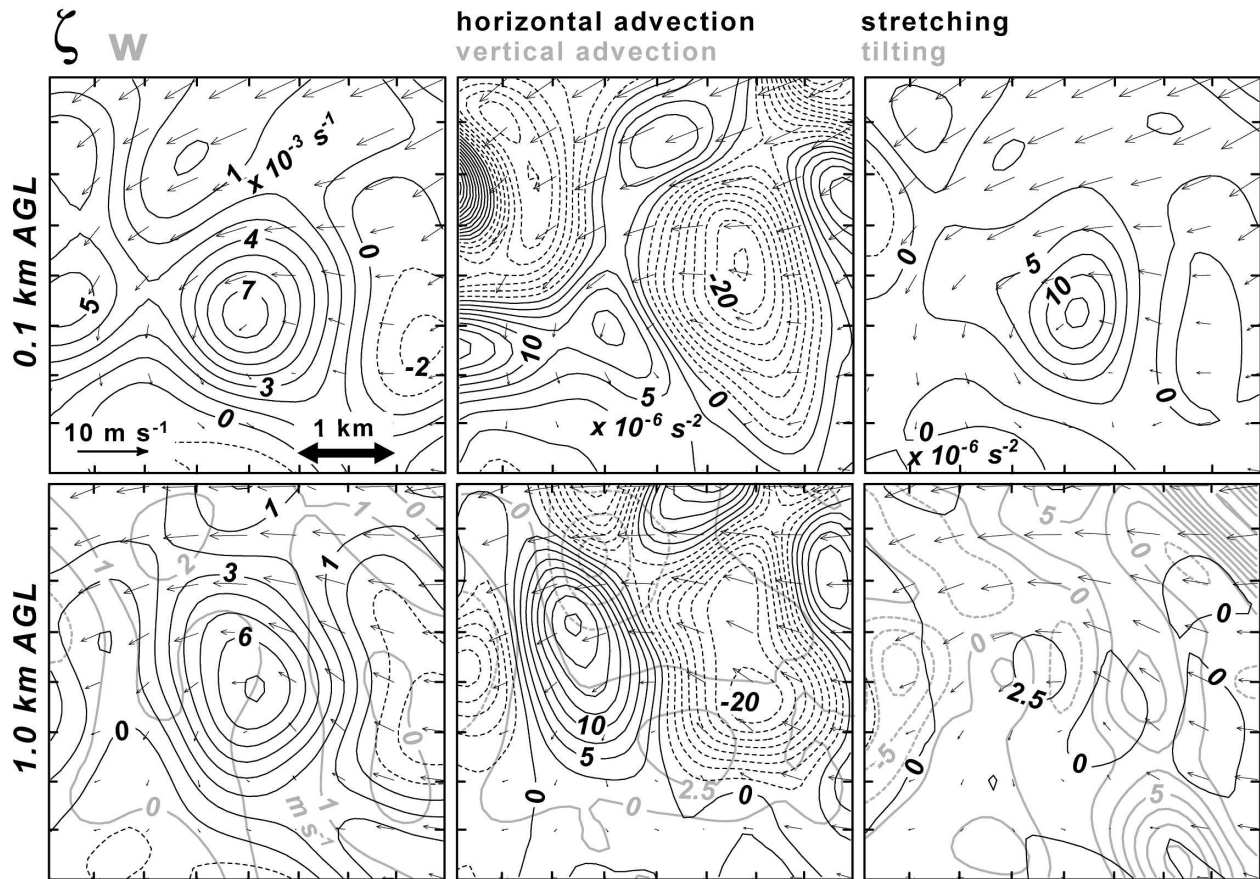
FIG. 12. As in Fig. 11, but for 2030 UTC (refer to Fig. 2).

maximum number 1 in Fig. 8). Furthermore, there are numerous absolute and relative helicity anomalies that exist in the absence of vertical vorticity anomalies. Much of the variability in the helicity fields, especially at 1.5 km, appears due to mesoscale influences rather than dynamics associated with the boundary layer thermals.

In addition to helicity, fields of eddy viscosity are examined in Fig. 10, whereby the eddy viscosity, K_m, is computed using

$$K_m = (k\Delta)^2 |\mathbf{D}|, \qquad (3)$$

where k is an empirical constant assigned to be 0.2 (Deardorff 1972), $\Delta = 100$ m is the grid length, and **D** is the deformation tensor (Smagorinsky 1963). The eddy viscosity fields also do not suggest a systematic reduction in the mixing coefficient within the cores of vorticity maxima. The helicity and eddy viscosity fields together indicate that it may be difficult to generalize

about the role of rotation in reducing mixing within updrafts.

5. Amplification and decay of the vertical vorticity extrema

As shown in section 3, vorticity extrema are observed to persist for the duration of the data collection period. For this reason, and also because the very definition of a vortex is ambiguous, it is not advisable to define a time of vortex genesis or demise. In fact, the evolution of the vorticity field documented in Figs. 2 and 3 may suggest that the very question of what leads to the genesis of boundary layer vortices might be ill posed, except perhaps in idealized simulations having a motionless initial state. Given these hurdles and uncertainties, our analysis in this section is limited to the conditions associated with the amplification and decay of *preexisting* vorticity extrema. Some commentary on the nature

2012 UTC   *Vorticity Maximum #5*
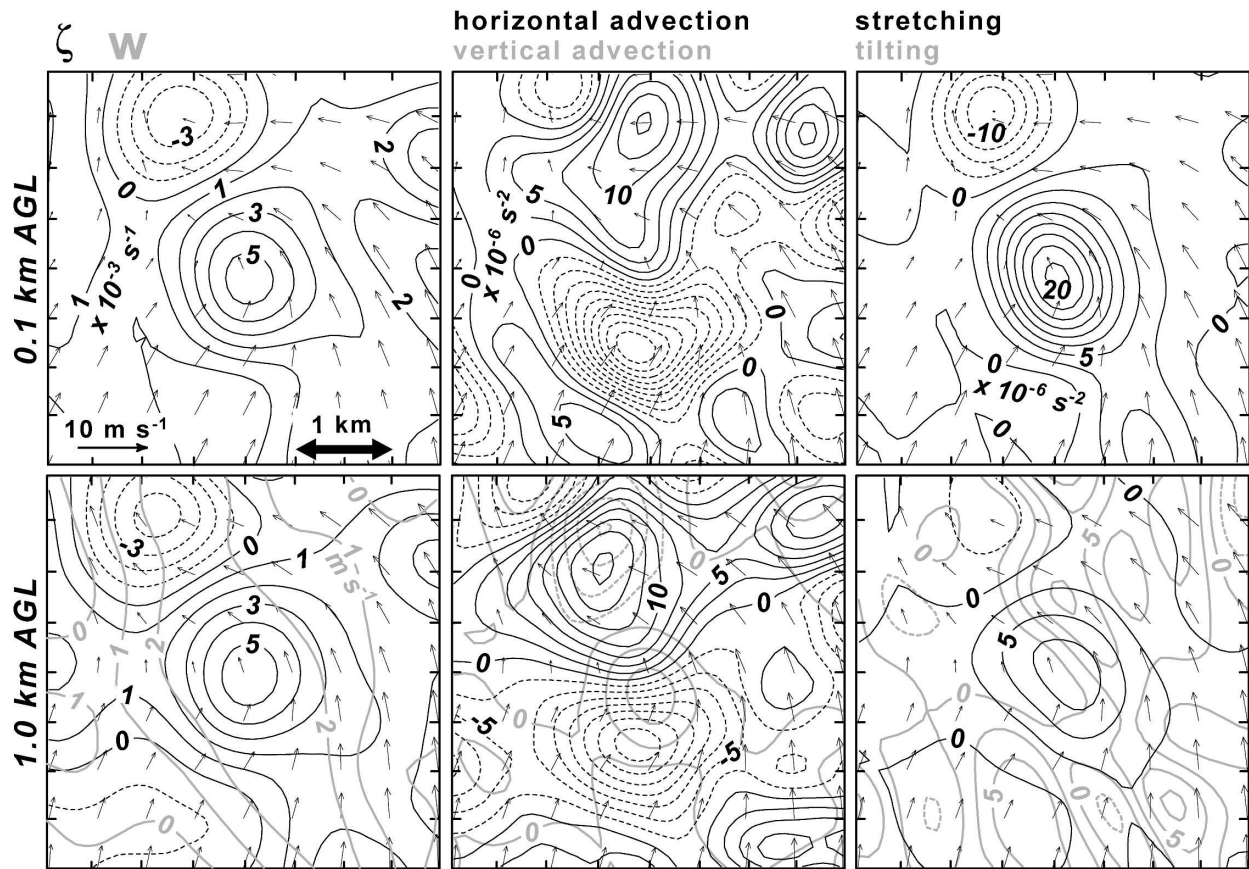
FIG. 13. As in Fig. 11, but for vorticity maximum number 5 (refer to Fig. 2).

of preexisting vorticity extrema is provided in the next section.

a. Vorticity amplification: Contributions to the local vorticity tendency

Neglecting curvature terms and molecular viscosity, the local vertical vorticity change is

$$
\frac{\partial \zeta}{\partial t} = \underbrace{-\mathbf{v}_h \cdot \boldsymbol{\nabla}(f + \zeta) - w\frac{\partial \zeta}{\partial z}}_{\text{horizontal and vertical advection}} \underbrace{-(f + \zeta)\boldsymbol{\nabla} \cdot \mathbf{v}_h}_{\text{stretching}}
$$
$$
+ \underbrace{\left(\frac{\partial u}{\partial z}\frac{\partial w}{\partial y} - \frac{\partial v}{\partial z}\frac{\partial w}{\partial x}\right)}_{\text{tilting}} + \underbrace{\left(\frac{\partial p}{\partial x}\frac{\partial \alpha}{\partial y} - \frac{\partial p}{\partial y}\frac{\partial \alpha}{\partial x}\right)}_{\text{solenoidal generation}}
$$
$$
+ \underbrace{\left(\frac{\partial F_y}{\partial x} - \frac{\partial F_x}{\partial y}\right)}_{\text{turbulent diffusion}}, \tag{4}
$$

where p is pressure, α is specific volume, f is the Coriolis parameter, and F_x and F_y represent turbulent diffusion of momentum in the x and y directions. The solenoidal term is neglected in our analysis. The term is zero if the anelastic approximation is made, and even in the worst case imaginable, with orthogonal isobars and isopycnics in a horizontal plane and with horizontal pressure and temperature gradients of 1 mb km^{-1} and 5 K km^{-1}, respectively, the term is of order 2×10^{-6} s^{-2}. The horizontal pressure and temperature gradients are about an order of magnitude smaller than the above estimates in the case at hand (Markowski et al. 2006). The diffusion of vorticity also is neglected in our analysis. In the past, a first-order or K-theory closure based on the Doppler-derived deformation has been applied in order to estimate turbulent diffusion (e.g., Brandes 1984a; Hane and Ray 1985), but the effect of vorticity diffusion on the vorticity evolution was found to be much smaller than the other terms (e.g., stretching and tilting; Brandes 1984a). Mixing effects may be more

2030 UTC   *Vorticity Maximum #5*
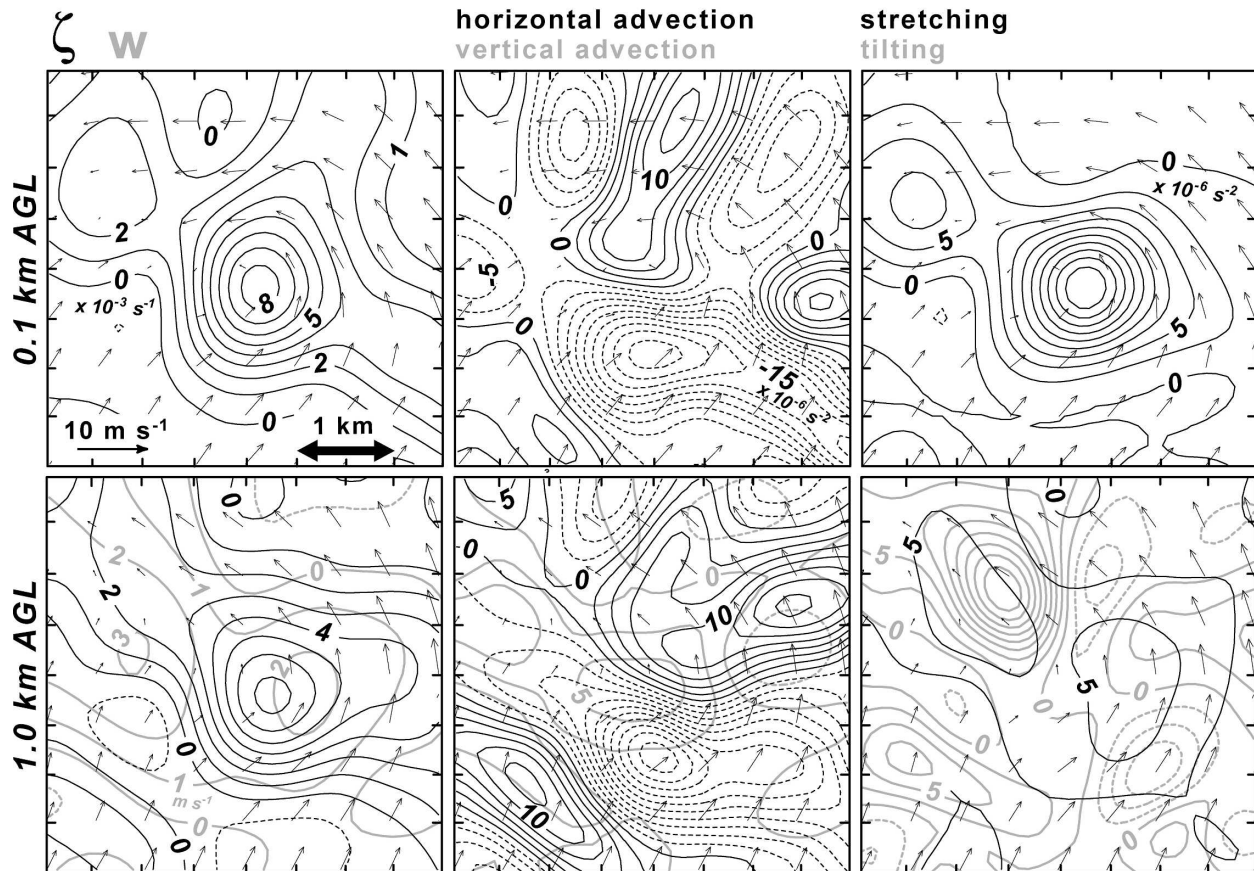
FIG. 14. As in Fig. 11, but for vorticity maximum number 5 at 2030 UTC (refer to Fig. 2).

significant in the surface layer where airflow deformation and vertical turbulent fluxes are large, but the surface layer is not well resolved by the radar observations.

An investigation of the dynamical processes associated with vorticity amplification is undertaken for vorticity maxima numbers 1 and 5. Vorticity maximum number 1 is located along the outflow boundary and undergoes a substantial amplification between 2012 and 2030 UTC, during which time the vertical vorticity increases from $\sim$0.002 to >0.007 s^{-1} (Figs. 11 and 12). Vorticity maximum number 5 was located in the warm sector south of the outflow boundary and intensifies from $\sim$0.005 to $\sim$0.009 s^{-1} during the same time period (Figs. 13 and 14).

Both vorticity maxima intensify upward from the surface (left panels of Figs. 11–14; also see Fig. 5). In both cases, horizontal advection and stretching are the largest contributors to the local vertical vorticity tendency at 0.1 km (e.g., top-center and top-right panels of Figs. 11–14). At 1.5 km, horizontal advection dominates

(bottom center of Figs. 11–14). The magnitude of the tilting term is large in both cases at 1.5 km, although not necessarily near the center of the vorticity maximum (bottom-right panels of Figs. 11–14). Once vertical vorticity begins to intensify near the surface, vertical advection also can become a significant contributor to the vorticity tendency in the middle boundary layer (bottom center of Figs. 13 and 14). Also note how the vertical velocity field is apparently altered by the intensification of vorticity maximum number 5 (bottom-left panels of Figs. 13 and 14).

In summary, at the start of the intensification periods (2012 UTC; Figs. 11 and 13), vorticity stretching is the largest contributor to the amplification of the vorticity maxima (advection cannot amplify vorticity extrema, only translate or reshape them). At the end of the periods of rapid intensification (2030 UTC; Figs. 12 and 14), when the vorticity maxima approximately reach their greatest amplitude, stretching is the largest contributor to vorticity amplification near the ground, and

Vorticity Maximum #1
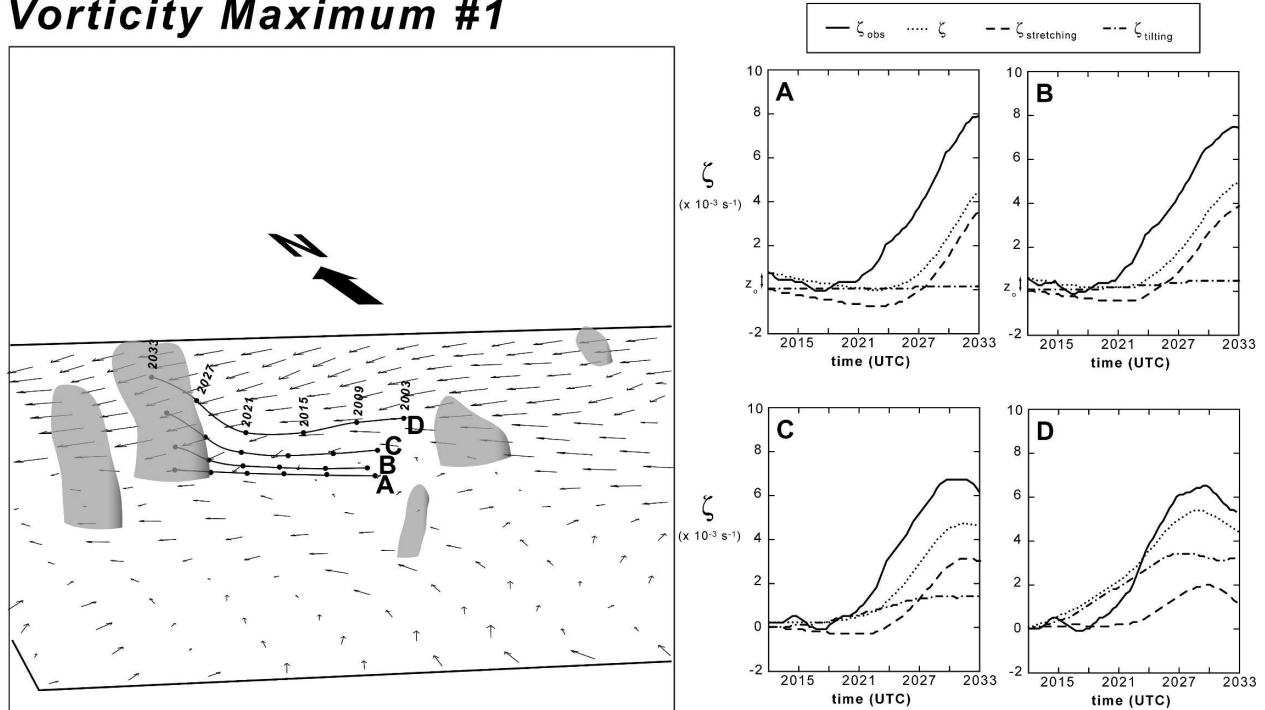
FIG. 15. (left) Trajectories entering vorticity maximum number 1 between 2003 and 2033 UTC. The four trajectories shown pass through the location of the maximum vertical vorticity at 0.1 km (trajectory "A"), 0.5 km (trajectory "B"), 1.0 km (trajectory "C"), and 1.5 km (trajectory "D"). Parcel locations at 6-min intervals along each trajectory are indicated (UTC time). The view is from the south. The arrows represent the horizontal wind vectors at 0.1 km and the gray surfaces are the 5×10^{-3} s^{-1} vertical vorticity isosurfaces. (right) The integrated contributions of vorticity stretching ($\zeta_{\text{stretching}}$) and tilting ($\zeta_{\text{tilting}}$) along trajectories A, B, C, and D, as a function of time. Neglecting turbulent diffusion, the total vertical vorticity following a parcel can be expressed as $\zeta = \zeta_{\text{o}} + \zeta_{\text{stretching}} + \zeta_{\text{tilting}}$, where ζ_{o} is the vertical vorticity of the air parcel at the start of the integration. The observed vertical vorticity along each trajectory, ζ_{obs}, also is plotted for comparison against ζ.

tilting is the largest contributor in the middle boundary layer (1.5 km), although mainly on the flanks of the vorticity maxima. It is worth noting that the terms producing the largest instantaneous vorticity tendencies do not necessarily contribute in the same proportion to the total integrated vorticity of the air parcels comprising the vorticity maxima, as will be shown in section 5c.

b. Vorticity amplification: Contributions to the Lagrangian vorticity tendency

To obtain perhaps a more complete understanding of the dynamical processes contributing to the amplification of vorticity extrema 1 and 5, the contributions to the Lagrangian vertical vorticity tendencies are examined for a number of trajectories entering vorticity maxima 1 and 5.[4] By integrating the Lagrangian form of

---

[4] "Lagrangian analysis" refers to an analysis following individual air parcels rather than following individual vorticity extrema.

(4), and neglecting the curvature, solenoidal, and turbulent diffusion terms as before, the vertical vorticity of a parcel, $\zeta(t)$, can be written as

$$\zeta(t) = \zeta_{\text{o}} - \int_{o}^{t} (f + \zeta)\boldsymbol{\nabla} \cdot \mathbf{v}_h \, dt'$$

$$+ \int_{o}^{t} \left(\frac{\partial u}{\partial z} \frac{\partial w}{\partial y} - \frac{\partial v}{\partial z} \frac{\partial w}{\partial x} \right) dt'$$

$$= \zeta_{\text{o}} + \zeta_{\text{stretching}} + \zeta_{\text{tilting}}, \quad (5)$$

where ζ_{o} is the vertical vorticity of the parcel at the start of the integration ($t = 0$) and $\zeta_{\text{stretching}}$ and ζ_{tilting} are the total contributions to ζ from stretching and tilting, respectively. Trajectories are computed using trilinear spatial interpolation and a fourth-order Runge–Kutta time integration algorithm using a time step of 10 s. The three-dimensional wind fields are assumed to vary linearly in time between the two Doppler analyses closest to the current time of a point along a trajectory. An error analysis of the trajectories is presented by Markowski et al. (2006).

Vorticity Maximum #5

FIG. 16. As in Fig. 15, but for vorticity maximum number 5. The view on the left is from the southwest.

Equation (5) is integrated along four trajectories for vorticity maxima 1 and 5 from 2012 to 2033 UTC. The four trajectories pass through the maximum vertical vorticity value at 2033 UTC at 0.1, 0.5, 1.0, and 1.5 km (trajectories "A," "B," "C," and "D," respectively; see Figs. 15 and 16). The differences between the observed vertical vorticity, ζ_{obs}, and $\zeta = \zeta_o + \zeta_{stretching} + \zeta_{tilting}$ are generally less than 2×10^{-3} s^{-1}. The largest disagreement between ζ_{obs} and $\zeta = \zeta_o + \zeta_{stretching} + \zeta_{tilting}$ ($\sim 4 \times 10^{-3}$ s^{-1}) is for the near-ground trajectories entering vorticity maximum number 1 (Fig. 15) and is perhaps due to inadequately resolved velocity gradients in that portion of the domain near the surface.

Along the near-ground trajectories entering vorticity maximum number 1 (trajectories "A" and "B" in Fig. 15), $\zeta_{stretching}$ is the dominant contributor to ζ, not surprisingly, since tilting goes to zero at the ground. For trajectories entering vorticity maximum number 1 at 1.0 and 1.5 km (trajectories "C" and "D" in Fig. 15), $\zeta_{tilting}$ assumes progressively larger roles, and in fact is the dominant contributor to ζ along trajectory "D." Curiously, for vorticity maximum number 5, $\zeta_{stretching}$ is the overwhelmingly dominant contributor to ζ along all four trajectories. The differences in the vorticity budgets of vorticity maxima 1 and 5 appear to be due to the fact that larger horizontal vorticity was available for tilting in the vicinity of vorticity maximum number 1,

which moves along the outflow boundary, where horizontal vorticity was enhanced. These results indicate that one cannot generalize when it comes to the dynamical processes responsible for the amplification of boundary layer vorticity extrema. Stretching virtually always will dominate near the surface, but above the surface the dominant contributors to vertical vorticity likely vary from case to case, or even from one vorticity extremum to another, as is observed here.

c. Observations of vertical vorticity decay

The processes associated with vorticity decay are examined for vorticity maximum 3 (refer to Figs. 2 and 3). Vorticity maximum number 3 weakens rapidly between 2100 and 2112 UTC, during which time the vertical voricity at 0.1 km decreases from ~ 0.009 to ~ 0.003 s^{-1} (Figs. 17 and 18). During the weakening phase, stretching provides a large negative contribution to the vertical vorticity tendency (Fig. 17), both at 0.1 and 1.5 km. The negative stretching contribution is a direct result of the development of a strong downdraft ($w < -2$ m s^{-1}) within the vorticity maximum (bottom-left panel of Fig. 17). The downdraft appears to be dynamically driven by the development of a downward-directed vertical pressure gradient within the vorticity maximum (Fig. 19), similar to the processes to which Klemp and Rotunno (1983) attributed occlusion downdraft formation

2100 UTC   *Vorticity Maximum #3*
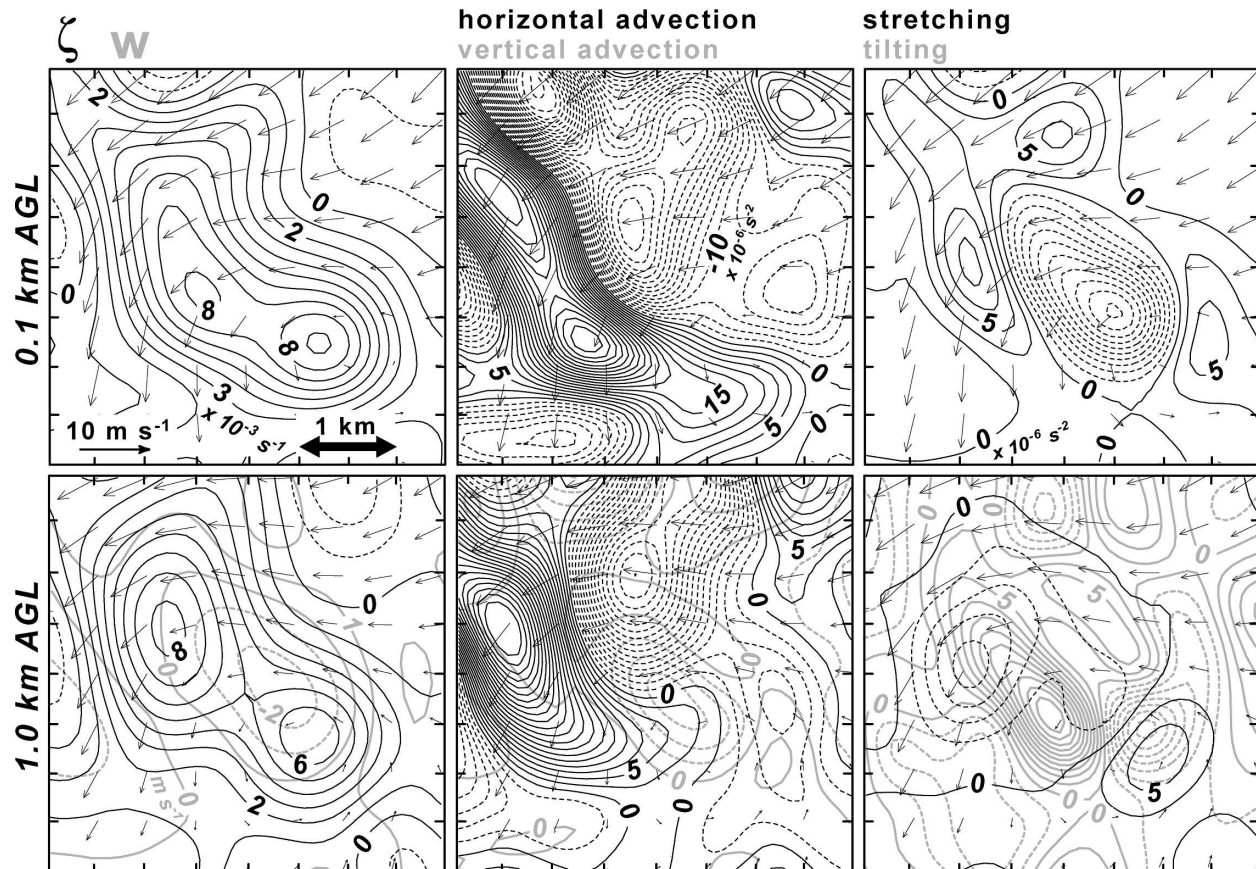
FIG. 17. As in Fig. 11, but for vorticity maximum number 3 at 2100 UTC (refer to Fig. 3).

in a supercell thunderstorm simulation. Carbone (1983) and Brandes (1984b) also observed a similar evolution within the parent circulations of a tornado, and similar processes were inferred by Mueller and Carbone (1987) in their observations of a downdraft within a vortex that developed along a thunderstorm gust front. This "updraft choking" mechanism also has been called the "vortex-valve effect" (Davies-Jones 1986), whereby the convergence associated with an updraft intensifies vertical vorticity from the bottom up, leading to an adverse vertical pressure gradient. When the adverse vertical pressure gradient owing to the vertical gradient of rotation becomes sufficiently large, the updraft weakens and may be replaced by a downdraft. The reversal in the sign of the vertical velocity also is associated with a change in the sign of the convergence, leading to the demise of the vorticity.

The case of the rapid weakening of vorticity maximum number 3 is an extreme example, but the weakening phases of several other vorticity maxima follow similar evolutions, whereby updraft weakening is associated with a downward-directed vertical pressure gradient force [e.g., vorticity maximum number 5 at 2042 UTC (Fig. 2); vorticity maximum 4 at 2118 UTC (Fig. 3)]. Even when there is no obvious suggestion of a rotation-induced, downward-directed vertical pressure gradient force, the weakening of vorticity maxima still is associated with negative stretching contributions to vorticity tendency and weakening updrafts, with the updraft weakening probably owing to either thermodynamical or other dynamical causes not induced by a vertical gradient of vertical vorticity.

6. Summary and conclusions

This paper has documented the evolution, characteristics, and dynamics of vertical vorticity extrema observed by mobile Doppler radars in a convective boundary layer during the 12 June 2002 IHOP deployment. The observations support the following conclusions:

2112 UTC   *Vorticity Maximum #3*
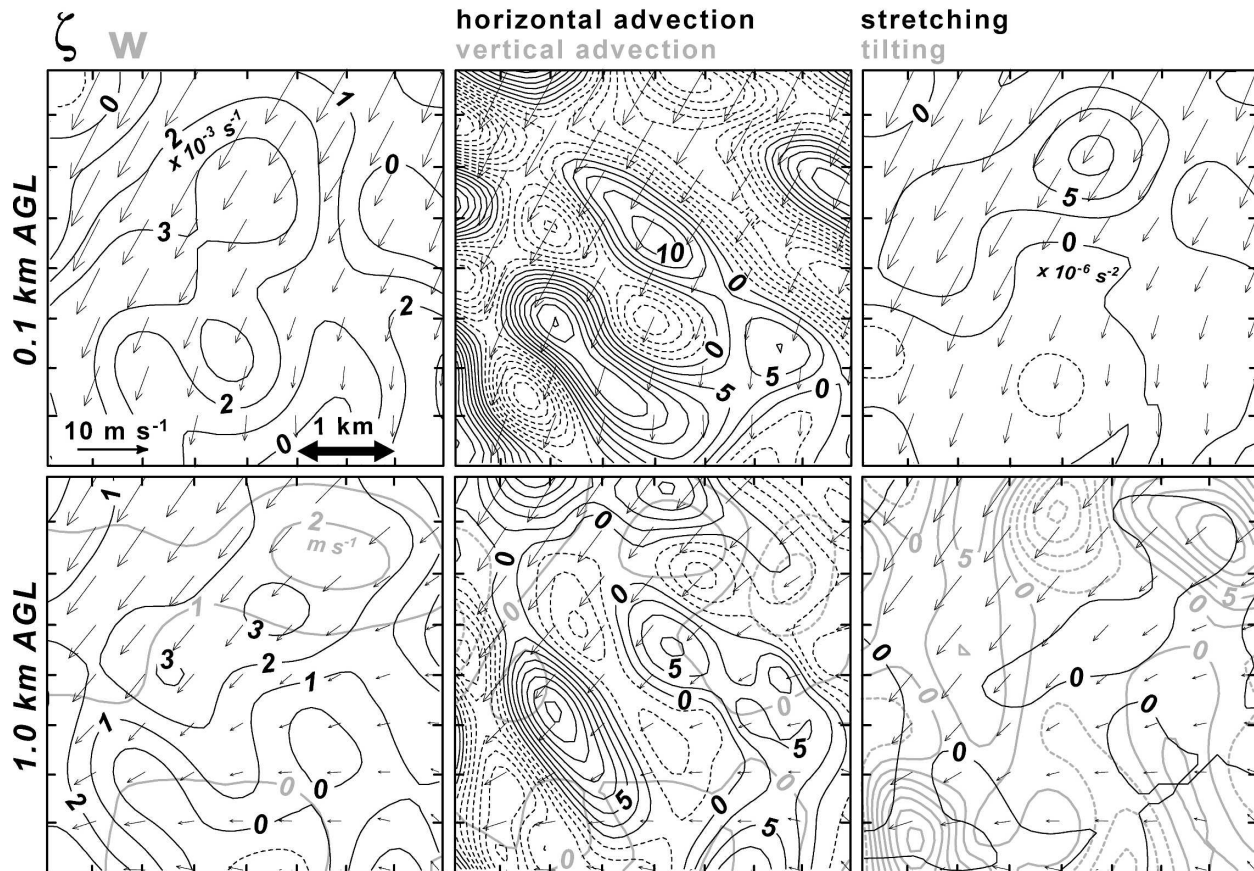
FIG. 18. As in Fig. 11, but for vorticity maximum number 3 at 2112 UTC (refer to Fig. 3).

1) The vertical vorticity field has remarkable time continuity, such that many vorticity extrema could be tracked continuously for the entire deployment spanning nearly 2 h.
2) The vertical vorticity extrema decrease in amplitude with height and are tilted by the vertical wind shear.
3) Periods of vertical vorticity amplification involve the superpositioning of an updraft; the air parcels comprising the vorticity maxima can acquire their vorticity from stretching or tilting, although the contributions can vary significantly from one vorticity maximum to another, and from one elevation to another, making it difficult to generalize about the dynamical processes responsible for the amplification of vorticity.
4) The vertical vorticity extrema are associated with pressure minima; given that the vorticity extrema weaken with height, vorticity extrema tend to be associated with a downward-directed vertical pressure gradient force.

5) Most of the vertical vorticity maxima weaken owing to weakening convergence; the demise of many strong vorticity maxima is brought about by the vortex-valve effect.
6) The interactions among vorticity extrema and between vertical vorticity extrema and the vertical velocity field are horribly complex; if such interactions are later shown to be crucial to convection initiation, it may be difficult to develop general guidelines for the prediction of convection initiation.
7) Not all vorticity extrema are associated with a reduction in mixing; the degree to which buoyancy dilution is inhibited, if at all, by rotation within an updraft depends on subtleties of the vorticity and velocity fields that vary from one vorticity extremum to another.

We have avoided one obvious question throughout: *What is the origin of vertical vorticity in the boundary layer?* The sequence of wind syntheses reveals that vor-
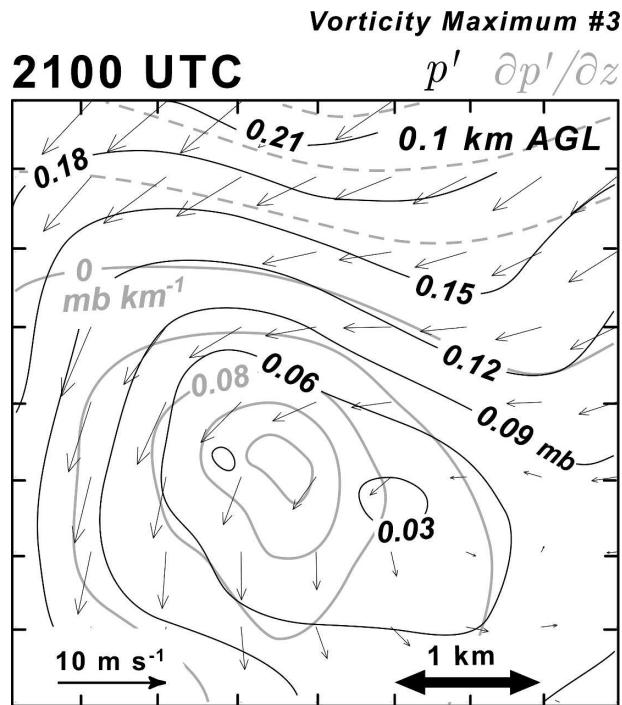
FIG. 19. Horizontal cross section of perturbation pressure, p', and the vertical perturbation pressure gradient, $\partial p'/\partial z$, at 0.1 km at 2100 UTC in the vicinity of vorticity maximum number 3 (refer to Fig. 3). The p' field is contoured in black at 0.03-mb intervals and the $\partial p'/\partial z$ is contoured in gray (negative contours are dashed) at 0.04 mb km^{-1} intervals. Perturbation pressures are with respect to the average pressure within the 10×10 km^2 domain at 0.1 km.

ticity anomalies can be tracked for long periods of time (>1 h). Many vorticity anomalies persisted for the entire data collection period, intensifying and weakening depending on the superpositioning of boundary layer drafts, to which the vorticity anomalies unavoidably feed back. Observationally, we cannot find some hypothetical initial time when $\zeta = 0$ everywhere.

Does surface friction play a role in generating vertical vorticity? How about slow, but nonzero baroclinic generation of vertical vorticity by horizontal solenoids possibly associated with thermals? Or horizontal vorticity generation by solenoids in the vertical plane, which subsequently can be tilted by gradients in the vertical motion field to produce vertical vorticity (e.g., Shapiro and Kanak 2002)? We do not have the data to address the contribution of surface friction to vertical vorticity, and it is questionable whether baroclinic effects could be observed adequately. In situ thermodynamic observations currently cannot sample thermodynamic fields with the level of detail to address baroclinic vorticity generation by thermals, and buoyancy fields retrieved from four-dimensional radar data are unavoidably noisy owing to the fact that they depend

on an extra (time) derivative of the velocity fields. Furthermore, there is the issue of how vertical vorticity arises at the surface. Davies-Jones (1982) argued that a downdraft is necessary for tornado formation in environments devoid of preexisting vertical vorticity at the surface. Are downdrafts in the convective boundary layer similarly necessary for vertical vorticity to arise at the surface?

In this case we cannot confidently say whether the development of the vorticity extrema was influenced by a shearing instability, in which a corridor of large vertical vorticity (or sheet of infinite vertical vorticity) along a wind shift line "breaks down" into a linear array of vorticity patches, with the spacing between vorticity patches dependent on the width of the initial corridor of vertical vorticity. This process is essentially a two-dimensional redistribution of vertical vorticity by way of horizontal advection. Admittedly, such a process may be difficult to observe, particularly if the initial corridor of vertical vorticity along the wind shift is narrow and therefore not well resolved. Furthermore, the process is not likely to be purely two-dimensional, owing to the presence of horizontal convergence along most wind shift lines; therefore, in practice, it may be difficult to attribute the development of vorticity patches to horizontal advection alone. Nonetheless, in some cases it seems that the circumstantial evidence implicates horizontal shearing instability as the cause for the development of vortices, for example, when the vortices are arranged along a well-defined wind shift line, with roughly equal spacing between vorticity centers (e.g., Mueller and Carbone 1987; Kingsmill 1995; Richardson et al. 2003). Even in these cases, however, some amplification of vorticity would likely occur either from stretching or tilting. In this 12 June 2002 case, several prominent vorticity maxima arose along the mesoscale wind shift associated with the outflow boundary, but their spacing was much more irregular than has been observed in the studies cited above. Many prominent vorticity maxima also developed away from the outflow boundary.

It is our hope that this work will stimulate additional observations of boundary layer vortices. The present study highlights some of the difficulties that may be faced in future studies attempting to relate boundary layer vortices to convection initiation. Some of the vorticity maxima observed herein had relatively large helicity and were associated with a suppression of mixing, while others were not. Furthermore, the dynamics associated with several of the vorticity maxima were found to weaken updrafts. In fact, there might be competing effects, as Davies-Jones (1986, p. 224) also noted in his commentary about thunderstorm updrafts: in-

creasing helicity might tend to reduce mixing and enhance an updraft, but such helicity amplifications might also be associated with a stronger adverse (downward directed) dynamic pressure gradient that would suppress updrafts. Another issue that might have to be addressed in the near future is what role, if any, vorticity extrema like those documented herein play in the formation of more intense geophysical vortices like dust devils and tornadoes. Vortices arising along horizontal wind shear lines have been found in prior studies to be "seedlings" for tornadoes in nonsupercell thunderstorms (Brady and Szoke 1989; Wakimoto and Wilson 1989; Roberts and Wilson 1995), but we cannot rule out that the ubiquitous boundary layer vorticity extrema documented herein may even have some role in tornado formation in supercell thunderstorms.

REFERENCES

Andrè, J. C., and M. LeSieur, 1977: Influence of helicity on the evolution of isotropic turbulence at high Reynolds number. *J. Fluid Mech.,* **18,** 187–207.

Arnott, N., Y. Richardson, J. Wurman, and J. Lutz, 2003: A solar calibration technique for determining mobile radar pointing angles. Preprints, *31st Int. Conf. on Radar Meteorology,* Seattle, WA, Amer. Meteor. Soc., 492–494.

Atkins, N. T., R. M. Wakimoto, and T. M. Weckwerth, 1995: Observations of the sea-breeze front during CaPE: Part II: Dual-Doppler and aircraft analysis. *Mon. Wea. Rev.,* **123,** 944–969.

——, ——, and C. L. Ziegler, 1998: Observations of the finescale structure of a dryline during VORTEX 95. *Mon. Wea. Rev.,* **126,** 525–550.

Barnes, S. L., 1964: A technique for maximizing details in numerical weather map analysis. *J. Appl. Meteor.,* **3,** 396–409.

Biggerstaff, M. I., and J. Guynes, 2000: A new tool for atmospheric research. Preprints, *20th Conf. on Severe Local Storms,* Orlando, FL, Amer. Meteor, Soc., 277–280.

Bluestein, H. B., C. C. Weiss, and A. L. Pazmany, 2004: Doppler radar observations of dust devils in Texas. *Mon. Wea. Rev.,* **132,** 209–224.

Brady, R. H., and E. J. Szoke, 1989: A case study of nonmesocyclone tornado development in northeast Colorado: Similarities to waterspout formation. *Mon. Wea. Rev.,* **117,** 843–856.

Brandes, E. A., 1984a: Vertical vorticity generation and mesocyclone sustenance in tornadic thunderstorms: The observational evidence. *Mon. Wea. Rev.,* **112,** 2253–2269.

——, 1984b: Relationships between radar-derived thermodynamic variables and tornadogenesis. *Mon. Wea. Rev.,* **112,** 1033–1052.

Carbone, R. E., 1983: A severe frontal rainband. Part II: Tornado parent vortex circulation. *Mon. Wea. Rev.,* **111,** 2639–2654.

Carroll, J. J., and J. A. Ryan, 1970: Atmospheric vorticity and dust devil rotation. *J. Geophys. Res.,* **75,** 5179–5184.

Cortese, T., and S. Balachandar, 1993: Vortical nature of thermal plumes in turbulent convection. *Phys. Fluids,* **A5,** 3226–3232.

Davies-Jones, R. P., 1982: A new look at the vorticity equation with application to tornadogenesis. Preprints, *12th Conf. on Severe Local Storms,* San Antonio, TX, Amer. Meteor. Soc., 249–252.

——, 1984: Streamwise vorticity: The origin of updraft rotation in supercell storms. *J. Atmos. Sci.,* **41,** 2991–3006.

——, 1986: Tornado dynamics. *Thunderstorm Morphology and Dynamics,* 2d ed., E. Kessler, Ed., University of Oklahoma Press, 197–236.

Deardorff, J. W., 1972: Numerical investigation of neutral and unstable planetary boundary layers. *J. Atmos. Sci.,* **29,** 91–115.

Fujiwhara, S., 1931: Short note on the behavior of two vortices. *Proc. Phys. Math. Soc. Japan,* **13,** 106–110.

Gal-Chen, T., 1978: A method for the initialization of the anelastic equations: Implications for matching models with observations. *Mon. Wea. Rev.,* **106,** 587–606.

——, and R. A. Kropfli, 1984: Buoyancy and pressure perturbations derived from dual-Doppler radar observations of the planetary boundary layer: Applications for matching models with observations. *J. Atmos. Sci.,* **41,** 3007–3020.

Hane, C. E., and P. S. Ray, 1985: Pressure and buoyancy fields derived from Doppler radar data in a tornadic thunderstorm. *J. Atmos. Sci.,* **42,** 18–35.

Hess, G. D., and K. T. Spillane, 1990: Characteristics of dust devils in Australia. *J. Appl. Meteor.,* **29,** 498–507.

Kanak, K. M., D. K. Lilly, and J. T. Snow, 2000: The formation of vertical vortices in the convective boundary layer. *Quart. J. Roy. Meteor. Soc.,* **126A,** 2789–2810.

Kaimal, J. C., and J. A. Businger, 1970: Case studies of a convective plume and a dust devil. *J. Appl. Meteor.,* **9,** 612–620.

Kessinger, C. J., P. S. Ray, and C. E. Hane, 1987: The Oklahoma squall line of 19 May 1977. Part I: A multiple Doppler analysis of convective and stratiform structure. *J. Atmos. Sci.,* **44,** 2840–2864.

Kingsmill, D. E., 1995: Convection initiation associated with a sea-breeze front, a gust front, and their collision. *Mon. Wea. Rev.,* **123,** 2913–2933.

Klemp, J. B., 1987: Dynamics of tornadic thunderstorms. *Annu. Rev. Fluid Mech.,* **19,** 369–402.

——, and R. Rotunno, 1983: A study of the tornadic region within a supercell thunderstorm. *J. Atmos. Sci.,* **40,** 359–377.

Koch, S. E., M. DesJardins, and P. J. Kocin, 1983: An interactive Barnes objective map analysis scheme for use with satellite

and conventional data. *J. Climate Appl. Meteor.,* **22,** 1487–1503.

Kundu, P. K., 1990: *Fluid Mechanics.* Academic Press, 638 pp.

Lee, B. D., and C. A. Finley, 2000: Simulating deep convection initiation by misocyclones. Preprints, *20th Conf. on Severe Local Storms,* Orlando, FL, Amer. Meteor. Soc., 70–73.

Lilly, D. K., 1986: The structure, energetics, and propagation of rotating convective storms. Part II: Helicity and storm stabilization. *J. Atmos. Sci.,* **43,** 126–140.

Lugt, H. J., 1979: The dilemma of defining a vortex. *Recent Developments in Theoretical and Experimental Fluid Mechanics,* U. Muller, K. G. Roesner, and B. Schmidt, Eds., Springer-Verlag, 309–321.

MacPherson, J. I., and A. K. Betts, 1997: Aircraft encounters with strong coherent vortices over the boreal forest. *J. Geophys. Res.,* **102** (D24), 29 231–29 234.

Markowski, P., C. Hannon, and E. Rasmussen, 2006: Observations of convection initiation "failure" from the 12 June 2002 IHOP deployment. *Mon. Wea. Rev.,* **134,** 375–405.

Matejka, T., 2002: Estimating the most steady frame of reference from Doppler radar data. *J. Atmos. Oceanic Technol.,* **19,** 1035–1048.

Maxworthy, T., 1973: A vorticity source for large scale dust devils and other comments on naturally occurring columnar vortices. *J. Atmos. Sci.,* **30,** 1717–1722.

Miles, J. W., and L. N. Howard, 1964: Note on a heterogeneous shearflow. *J. Fluid Mech.,* **20,** 331–336.

Mueller, C. K., and R. E. Carbone, 1987: Dynamics of a thunderstorm outflow. *J. Atmos. Sci.,* **44,** 1879–1898.

Pietrycha, A. E., and E. N. Rasmussen, 2004: Finescale surface observations of the dryline: A mobile mesonet perspective. *Wea. Forecasting,* **19,** 1075–1088.

Richardson, Y. P., J. M. Wurman, and C. Hartman, 2003: Multi-Doppler analysis of convective initiation on 19 June 2002 during IHOP. Preprints, *31st Int. Conf. on Radar Meteorology,* Seattle, WA, Amer. Meteor. Soc., 793–795.

Roberts, R. D., and J. W. Wilson, 1995: The genesis of three non-supercell tornadoes observed with dual-Doppler radar. *Mon. Wea. Rev.,* **123,** 3408–3436.

Roux, F., 1985: Retrieval of thermodynamic fields from multiple-Doppler radar data using the equations of motion and the thermodynamic equation. *Mon. Wea. Rev.,* **113,** 2142–2157.

Schneider, J. M., and D. K. Lilly, 1999: An observational and numerical study of a sheared, convective boundary layer. Part I: Phoenix II observations, statistical description, and visualization. *J. Atmos. Sci.,* **56,** 3059–3078.

Segal, M., and R. W. Arritt, 1992: Nonclassical mesoscale circulations caused by surface sensible heat-flux gradients. *Bull. Amer. Meteor. Soc.,* **73,** 1593–1604.

Shapiro, A., and K. M. Kanak, 2002: Vortex formation in ellipsoidal thermal bubbles. *J. Atmos. Sci.,* **59,** 2253–2269.

Smagorinsky, J., 1963: General circulation experiments with the primitive equations. Part I: The basic experiment. *Mon. Wea. Rev.,* **91,** 99–164.

Snow, J. T., and T. M. McClelland, 1990: Dust devils at White Sands Missile Range, New Mexico. Part I: Temporal and spatial distribution. *J. Geophys. Res.,* **95,** 13 707–13 721.

Trapp, R. J., and C. A. Doswell, 2000: Radar data objective analysis. *J. Atmos. Oceanic Technol.,* **17,** 105–120.

Wakimoto, R. M., and J. W. Wilson, 1989: Non-supercell tornadoes. *Mon. Wea. Rev.,* **117,** 1113–1140.

Weckwerth, T. M., and Coauthors, 2004: An overview of the International H$_2$O Project (IHOP) and some preliminary highlights. *Bull. Amer. Meteor. Soc.,* **85,** 253–277.

Wilson, J. W., G. B. Foote, N. A. Crook, J. C. Fankhauser, C. G. Wade, J. D. Tuttle, and C. K. Mueller, 1992: The role of boundary-layer convergence zones and horizontal rolls in the initiation of thunderstorms: A case study. *Mon. Wea. Rev.,* **120,** 1785–1815.

Wurman, J. M., J. M. Straka, E. N. Rasmussen, M. Randall, and A. Zahrai, 1997: Design and deployment of a portable, pencil-beam, pulsed, 3-cm Doppler radar. *J. Atmos. Oceanic Technol.,* **14,** 1502–1512.